Lattice study of a magnetic contribution to heavy quark momentum diffusion

D. Banerjee,[a,b] **S. Datta**[c] **and M. Laine**[d]

[a] *Saha Institute of Nuclear Physics,*
1/AF Bidhannagar, Kolkata 700064, India

[b] *Homi Bhabha National Institute, Training School Complex,*
Anushaktinagar, Mumbai 400094, India

[c] *Department of Theoretical Physics, Tata Institute of Fundamental Research,*
Homi Bhabha Road, Mumbai 400005, India

[d] *AEC, Institute for Theoretical Physics, University of Bern,*
Sidlerstrasse 5, CH-3012 Bern, Switzerland

E-mail: debasish.banerjee@saha.ac.in, saumen@theory.tifr.res.in,
laine@itp.unibe.ch

ABSTRACT: Heavy quarks placed within a hot QCD medium undergo Brownian motion, characterized by specific transport coefficients. Their determination can be simplified by expanding them in T/M, where T is the temperature and M is a heavy quark mass. The leading term in the expansion originates from the colour-electric part of a Lorentz force, whereas the next-to-leading order involves the colour-magnetic part. We measure a colour-magnetic 2-point correlator in quenched QCD at $T \sim (1.2 - 2.0)T_{\rm c}$. Employing multilevel techniques and non-perturbative renormalization, a good signal is obtained, and its continuum extrapolation can be estimated. Modelling the shape of the corresponding spectral function, we subsequently extract the momentum diffusion coefficient, κ. For charm (bottom) quarks, the magnetic contribution adds $\sim 30\%$ (10%) to the electric one. The same increases apply also to the drag coefficient, η. As an aside, the colour-magnetic spectral function is computed at NLO.

Contents

1 Introduction

Thanks to the inertia provided by their mass, heavy quarks tend to interact less efficiently with a hot QCD medium than light quarks or gluons. This turns them into a tractable probe for the properties of the strongly interacting plasma that is generated in heavy ion collision experiments, a fact that has inspired theoretical and phenomenological investigations of a broad variety (cf., e.g., ref. [1] for a review).

A quantitative study of the movement of heavy quarks within an expanding hydrodynamical background can be based on the Langevin equation [2, 3],

$$\dot{p}_i(t) = -\eta\, p_i(t) + \xi_i(t)\,, \quad \langle \xi_i(t) \rangle = 0\,, \quad \langle \xi_i(t')\, \xi_j(t) \rangle = \kappa\, \delta_{ij}\, \delta(t - t')\,, \qquad (1.1)$$

where the p_i denote components of momenta. The magnitude of the kicks that the medium exerts are incorporated in the autocorrelator of the stochastic noise, parametrized by the momentum diffusion coefficient, κ. Thanks to a fluctuation-dissipation relation (cf. eq. (5.8)), κ in turn determines the drag coefficient, η, which according to eq. (1.1) can be interpreted as a kinetic equilibration rate.

A QCD-based determination of κ can be simplified by viewing it as an expansion in T/M, where T is the temperature and M is a heavy quark mass. The leading term, which remains present in the asymptotic limit of a very small T/M, originates from a colour-electric

two-point correlator [4, 5]. Let us denote this term by κ_E. Many lattice studies of κ_E have been reported in quenched QCD [6–12], and even though further improvements are desirable, related for instance to non-perturbative renormalization, unquenching, and analytic continuation, the patterns that have emerged so far point towards a consistent picture.

In view of the fact that the charm quark is not extremely heavy it can be asked, however, how large the corrections from a finite T/M could be. It turns out that there are a number of separate contributions at this order, and a particularly important one originates from the magnetic part of a coloured Lorentz force [13]. The colour-magnetic contribution experiences non-trivial renormalization [14], but otherwise its lattice determination should not be harder than for the colour-electric case. Indeed attempts in this direction have been initiated by several groups recently [15, 16].

The goal of the present paper is to study the colour-magnetic contribution to heavy quark momentum diffusion through moderate-scale lattice simulations. On the theoretical side, a significant part of the effort goes to clarifying the renormalization of the observable, which we aim to accomplish (partly) on the non-perturbative level. On the physics side, different orders in T/M permit for interesting comparisons of the charm and bottom quark properties.

Our presentation is organized as follows. After formulating the basic framework (cf. section 2), we specify its lattice implementation and the set of simulations carried out (cf. section 3). Data analysis is split into two parts, an in principle well-defined continuum extrapolation in the imaginary-time domain (cf. section 4), as well as a spectral analysis in the Minkowskian one, which is necessarily of a more exploratory nature (cf. section 5). In spite of the systematic uncertainties of the latter step, the results show a coherent pattern, and permit for us to formulate physical conclusions (cf. section 6). Technical details, related to non-perturbative renormalization, tree-level improvement, next-to-leading order corrections to the colour-magnetic spectral function, and fitting strategies, are relegated to appendices A, B, C and D, respectively.

2 Basic framework

The correlation function that we are concerned with can formally be expressed as [13]

$$[G_B(\tau)]_{\text{bare}} \equiv \frac{\sum_i \text{Re Tr} \langle U(1/T;\tau) \, [gB_i(\tau)]_{\text{bare}} \, U(\tau;0) \, [gB_i(0)]_{\text{bare}} \rangle}{3 \, \text{Re Tr} \langle U(1/T;0) \rangle} \,. \tag{2.1}$$

Here $\tau \in (0, 1/T)$ is an imaginary-time coordinate; $U(\tau_2; \tau_1)$ is a straight Wilson line in the time direction; and gB_i represents a colour-magnetic field strength, defined as a Hermitean matrix transforming in the adjoint representation.

In order to measure eq. (2.1) on the lattice (L), we make use of the Wilson gauge action. The magnetic field is defined as

$$[gB_i]_{\text{bare,L}} \equiv \frac{\sum_{j,k} \epsilon_{ijk} \widehat{F}_{jk}}{2\imath} \,, \tag{2.2}$$

where $\imath$ is the imaginary unit and $\widehat{F}_{jk}$ is a field strength obtained from a clover,

$$\widehat{F}_{jk}(x) \equiv \frac{Q_{jk}(x) - Q_{kj}(x)}{8a^2} \,, \tag{2.3}$$

$$Q_{jk}(x) \equiv P_{jk}(x) + P_{k-j}(x) + P_{-j-k}(x) + P_{-kj}(x) \,, \tag{2.4}$$

where $P_{jk}(x) \equiv U_j(x)\, U_k(x+a\hat{j})\, U_j^\dagger(x+a\hat{k})\, U_k^\dagger(x)$ is a plaquette; U_j is a link matrix pointing in the j-direction; $U_{-j}(x) \equiv U_j^\dagger(x - a\hat{j})$; $\hat{j}$ is a unit vector; and a is the lattice spacing.

At loop level, the colour-magnetic field experiences non-trivial renormalization [17]. In dimensional regularization (DR), this means that the bare correlator needs to be multiplied by a renormalization factor in order to obtain a finite $\overline{\mathrm{MS}}$ correlator,

$$[G_B(\tau)]_{\mathrm{renorm},\bar{\mu}} = \left[1 + \frac{g^2 \mu^{-2\epsilon}}{(4\pi)^2} \frac{N_{\mathrm{c}}}{\epsilon} + \mathcal{O}(g^4) \right]^2 [G_B(\tau)]_{\mathrm{bare,DR}} \,, \tag{2.5}$$

where $g^2 = 4\pi\alpha_{\mathrm{s}}$ is a renormalized coupling, μ is a scale parameter, $N_{\mathrm{c}} = 3$, and the space-time dimension has been written as $D = 4 - 2\epsilon$. Because of this renormalization, the correlator now depends on the $\overline{\mathrm{MS}}$ renormalization scale, $\bar{\mu}^2 \equiv 4\pi\mu^2 e^{-\gamma_{\mathrm{E}}}$. In physical results, the correlator is multiplied by a Wilson coefficient, which cancels the scale dependence.

Considering the Lorentz force that acts on heavy quarks, and matching a full thermal QCD computation onto a static effective theory one, the Wilson coefficient relevant for the colour-magnetic correlator was determined in ref. [14]. Concretely, we can write

$$[G_B(\tau)]_{\mathrm{physical}} = c_B^2(\bar{\mu})\, [G_B(\tau)]_{\mathrm{renorm},\bar{\mu}} \,, \tag{2.6}$$

$$c_B(\bar{\mu}) = 1 + \frac{g^2 N_{\mathrm{c}}}{8\pi^2} \left[\ln\left(\frac{\bar{\mu} e^{\gamma_{\mathrm{E}}}}{4\pi T} \right) - 1 \right] + \mathcal{O}(g^4) \,. \tag{2.7}$$

The information in eq. (2.7) can be rephrased by running $\overline{\mathrm{MS}}$ operators to the scale [14]

$$\bar{\mu} \approx 19.179 T \,, \tag{2.8}$$

where the square bracket in eq. (2.7) vanishes. We note that this is a remarkably large scale, suggesting a reasonable convergence down to fairly low temperatures.

After the establishment of eq. (2.8), the remaining challenge is to convert the lattice operator in eq. (2.2) into the $\overline{\mathrm{MS}}$ scheme. This problem has been addressed in ref. [18], in the context of a spin-dependent operator involving the magnetic field [17]. The procedure involves the use of a finite-volume scheme with Schrödinger functional (SF) boundary conditions; the conversion of those results into a renormalization group invariant (RGI) operator; and a subsequent relation of the RGI operator to the $\overline{\mathrm{MS}}$ one at the scale $\bar{\mu}$. The conversions are achieved by multiplying the physical correlation function by ratios of unphysical but technically more accessible auxiliary correlation functions, denoted below by Φ, which can be determined in different renormalization schemes. The ingredients are described in more detail in appendix A. The end result can be expressed as

$$\frac{[G_B(\tau)]_{\mathrm{physical}}}{[G_B(\tau)]_{\mathrm{bare,L}}} = \left\{ \frac{\Phi_{\overline{\mathrm{MS}}}(\bar{\mu} = 19.179 T)}{\Phi_{\mathrm{RGI}}} \times \frac{\Phi_{\mathrm{RGI}}}{\Phi_{\mathrm{SF}}(\frac{1}{2L_{\mathrm{max}}})} \times Z_{\mathrm{spin}}^{\mathrm{SF}}(2L_{\mathrm{max}}) \right\}^2 \,, \tag{2.9}$$

where the separate factors originate from eqs. (A.1) and (A.7).

β	N_τ	N_s	subs	sub-ups	confs	streams	τ_{int}	r_0/a	T/T_c
6.860	20	48	5	500	500	5	13	17.7	1.19
	20	56	5	500	905	5	13	17.7	1.19
	20	64	5	500	1020	6	11	17.7	1.19
7.010	24	64	6	500	1465	10	7	21.3	1.19
	24	72	6	500	1051	15	4	21.3	1.19
7.050	20	48	5	500	875	4	5	22.4	1.50
	20	56	5	500	706	5	5	22.4	1.50
	20	64	5	500	1000	8	8	22.4	1.50
7.135	28	84	7	1000	1225	9	11	24.8	1.19
7.192	24	60	4	500	1530	9	5	26.6	1.48
	24	72	4	500	1448	7	5	26.6	1.48
	30	96	5	1000	1256	12	12	26.6	1.19
7.300	20	48	4	500	1000	4	5	30.2	2.03
	20	64	4	500	1120	8	5	30.2	2.03
7.330	28	84	7	1000	1256	10	11	31.3	1.50
7.457	24	60	4	500	1645	9	4	36.4	2.04
	24	72	4	500	1038	7	4	36.4	2.04
7.634	30	96	5	1000	1130	9	7	44.9	2.01

Table 1. The lattices simulated (coupling $\beta = 6/g_0^2$, geometry $N_\tau \times N_s^3$), together with sublattices (subs), sublattice updates (sub-ups), statistics (confs), streams, integrated autocorrelation times (τ_{int}), and physical scales (r_0/a [20], T/T_c [21]). The last two are estimated as explained below eq. (3.1).

We end this section by noting that, numerically, the renormalization factor in eq. (2.9) is fairly large. Typical values entering our analysis are $\{\ldots\}^2 \approx 3.12$ for $\beta \approx 7.0$ and $T \approx 1.2 T_c$, or $\{\ldots\}^2 \approx 2.87$ for $\beta \approx 7.6$ and $T \approx 2.0 T_c$.

3 Numerical implementation

We now proceed with the numerical measurement of the correlation function defined by eqs. (2.1)–(2.4). The measurements are carried out in quenched QCD, with the Wilson gauge action, parametrized by a bare coupling $\beta = 6/g_0^2$. The β values and lattice volumes are assembled in table 1. We note that spectral studies necessitate a large number of temporal points and correspondingly fine lattices (large values of β). As a consequence our physical volumes are small compared with the state-of-the-art [19], nevertheless the finite-volume effects appear to be somewhat smaller than statistical uncertainties (see below).

For a conversion to physical units [20], we have employed the interpolating function

$$\ln\left(\frac{r_0}{a}\right) = \left[\frac{\beta}{12 b_0} + \frac{b_1}{2 b_0^2} \ln\left(\frac{6 b_0}{\beta}\right)\right] \frac{1 + c_1/\beta + c_2/\beta^2}{1 + c_3/\beta + c_4/\beta^2}, \quad b_0 \equiv \frac{11}{(4\pi)^2}, \quad b_1 \equiv \frac{102}{(4\pi)^4}, \quad (3.1)$$

inserting updated coefficients for large β from the caption of table 2 of ref. [22], viz.

$$c_1 = -8.9664, \quad c_2 = 19.21, \quad c_3 = -5.25217, \quad c_4 = 0.606828. \quad (3.2)$$

Conversions to units of T_c make use of $r_0 T_c = 0.7457(45)$ from ref. [21].

As far as the Monte Carlo update goes, the lattice was divided into sublattices along the τ direction, in accordance with the multilevel philosophy [23, 24]. Additional sublattice updates were performed. Each update consisted of 1 heatbath step followed by 3 over-relaxation steps. We started a number of streams for each parameter set, with different pseudorandom number chains. The runs were started from a cold configuration, in order to give the Polyakov loop a real expectation value and to stay in the sector of trivial topology.

To probe the efficiency of the update, we calculated an integrated autocorrelation time, τ_{int}, for the absolute value of the Polyakov loop. Data from different streams were combined according to ref. [25]. The integration extended to a time interval in which the autocorrelation function had not decreased below 10^{-3} of its original value. Sufficient thermalization was allowed for ($\gg 100\tau_{\text{int}}$). The parameters of the runs are listed in table 1.

We also looked at autocorrelations in the numerator of $G_B(\tau)$ (cf. eq. (2.1)). For small τ, we got autocorrelation times similar to those from the Polyakov loop. For larger τ, the measurement of the autocorrelation function became noisy, however as long as a signal could be obtained, the autocorrelation time decreased rather than increased with τ.

A much longer autocorrelation time is known to characterize the topological charge, Q [26]. We checked its movement on some of our lattices, defining Q via gradient flow [27]. Our lattices are at high temperatures, where the physical topological susceptibility becomes vanishingly small. Starting from a configuration with all links set to unity, we found that Q sticks to the trivial sector. We also checked that the final configurations for these sets are at $Q = 0$. This suggests that our configurations were stuck in the trivial sector all along.

The values of τ_{int} as indicated in table 1 were taken as estimators of the autocorrelations in the data. Subsequently the data was blocked in block sizes $\gtrsim 2\tau_{\text{int}}$, and the blocked data was considered independent in the bootstrap analysis.

4   Data and its analysis

The methods and statistics described in the previous section lead to a good signal for the observable in eq. (2.1), in the temperature range indicated in table 1. In this section we explain how we have estimated the infinite-volume and continuum limits of this data set.

In order to show the results of the measurements, we normalize them to the correlator obtained with tree-level lattice perturbation theory, cf. eq. (B.3). Results from different volumes are shown in figure 1. We observe no appreciable evolution at $N_s \gtrsim 3N_\tau$, and conclude that such results reasonably approximate the infinite-volume limit within statistical uncertainties, even if our volumes are admittedly small in physical units.

In order to extrapolate to continuum, the bare data need to be multiplied with the renormalization factor from eq. (2.9). In figure 2, we show results from different lattice spacings (at more or less fixed aspect ratios). Only modest lattice spacing dependence can be discerned within the statistical uncertainties.

To accelerate the approach to the continuum limit, we have assigned the bare lattice data to tree-level improved distances [20, 28] (cf. appendix B), denoted by $\bar{\tau}$ in figures 1 and 2. The data at the coarser lattices are B-spline interpolated (or in single cases, extrapolated)
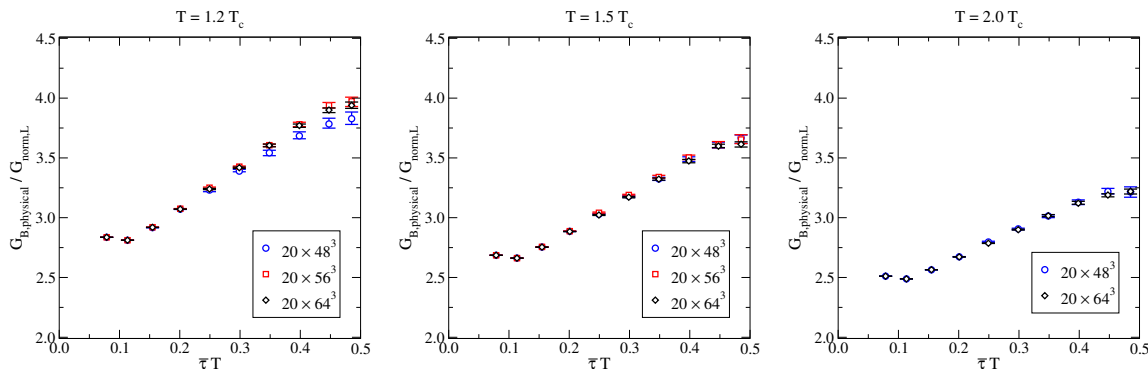
Figure 1. Illustration of the volume dependence of the renormalized correlator (cf. eq. (2.9)) at $T \approx 1.2T_c$ (left), $1.5T_c$ (middle), and $2.0T_c$ (right), after normalization to eq. (B.3). By $\overline{\tau}$ we denote an improved distance, as defined in eq. (B.4).
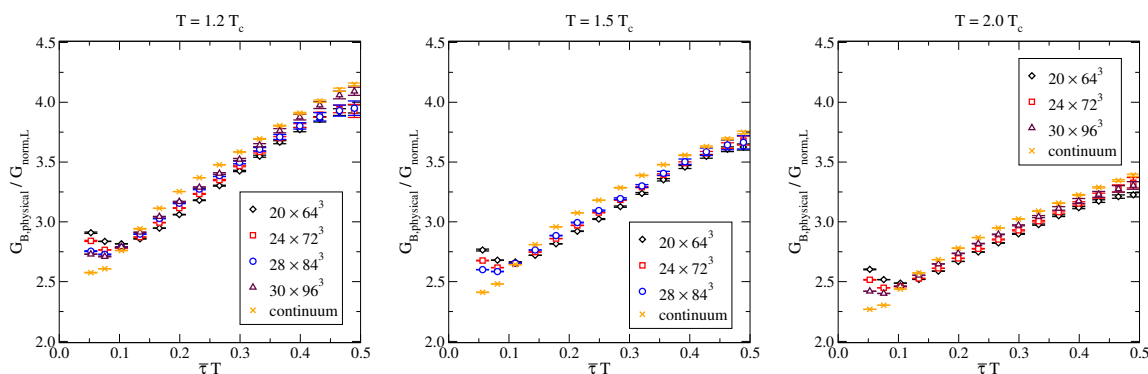

Figure 2. Illustration of the approach of the renormalized correlator (cf. eq. (2.9)) to the continuum limit, at $T \simeq 1.2T_c$ (left), $1.5T_c$ (middle), and $2.0T_c$ (right), after normalization to eq. (B.3). Data at the coarser lattices have been interpolated to the distances of the finest lattice.

to the improved distances of the finest lattice. Subsequently fits linear in $1/N_\tau^2$ are carried out. The extrapolation results are shown in figure 2 with the crosses.

Finally, the ratio obtained is multiplied by the continuum version of eq. (B.3), viz.

$$G_{\mathrm{norm,DR}}(\tau) \equiv \pi^2 T^4 \left[\frac{\cos^2(\pi\tau T)}{\sin^4(\pi\tau T)} + \frac{1}{3\sin^2(\pi\tau T)} \right] . \tag{4.1}$$

Thereby we obtain an estimate of the continuum colour-magnetic correlator that can be subjected to a spectral analysis.

5 Implications for heavy quark momentum diffusion

Having estimated the continuum limit of G_B in the previous section, the remaining challenge is to extract the momentum diffusion coefficient from this data. If the continuum correlator is expressed in a spectral representation,

$$[G_B(\tau)]_{\mathrm{physical}} \equiv \int_0^\infty \frac{\mathrm{d}\omega}{\pi} \rho_B(\omega) \frac{\cosh\left[\left(\frac{1}{2T} - \tau\right)\omega\right]}{\sinh\left(\frac{\omega}{2T}\right)} , \tag{5.1}$$

then κ_B is given by

$$\kappa_B = \lim_{\omega \to 0} \frac{2T\rho_B(\omega)}{\omega}\,. \tag{5.2}$$

The procedure that we adopt for extracting κ_B goes through modelling the shape of ρ_B. Similarly to the colour-electric spectral function [29], we do not expect ρ_B to contain any sharp transport peak at $\omega \ll T$. Then, its infrared (IR) part can be approximated as

$$\phi_{\mathrm{IR}}(\omega) \equiv \frac{\kappa_B\,\omega}{2T}\,. \tag{5.3}$$

For the ultraviolet (UV) part, we adopt the vacuum-like ansatz

$$\phi_{\mathrm{UV}}(\omega) \equiv \frac{g^2(\bar{\mu}_B)\,C_{\mathrm{F}}\,\omega^3}{6\pi}\,, \quad \bar{\mu}_B \equiv \max\left[\omega^{1-\frac{\gamma_0}{b_0}}\,(\pi T)^{\frac{\gamma_0}{b_0}}, \pi T\right], \tag{5.4}$$

where $C_{\mathrm{F}} \equiv (N_c^2 - 1)/(2N_c)$ and, for $\{N_c, N_{\mathrm{f}}\} = \{3, 0\}$, the colour-magnetic anomalous dimension is $\gamma_0 \equiv 3/(8\pi^2)$ (cf. appendix A), and $b_0 = 11/(16\pi^2)$.[1] In the colour-electric case, γ_0 is absent [30], whereby $\bar{\mu}_E \equiv \max(\omega, \pi T)$. The model spectral function is defined as

$$\rho_B(\omega) \equiv \sqrt{\phi_{\mathrm{IR}}^2(\omega) + a_B\,\phi_{\mathrm{UV}}^2(\omega)}\,, \tag{5.5}$$

where $a_B \simeq 1$ is treated as a fit parameter. This type of a model, together with many other shapes,[2] were explored for the colour-electric case in ref. [9]. The results were found to lie around the middle of an admissible range, even if the systematic uncertainties are underestimated by the very constrained ansatz of eq. (5.5).

Inserting eq. (5.5) into eq. (5.1), $G_B(\tau)$ is a function of two parameters, κ_B and a_B. We fit the result to both finite-a and to the continuum-extrapolated data sets in the range $\tau \geq \tau_{\min} \in (0.20 - 0.35)/T$, with $\tau_{\min}$ chosen so as to obtain good $\chi^2/\mathrm{d.o.f.}$ Error estimates are based on a bootstrap analysis on the blocked data (cf. section 3), with correlations in the data at different values of τ accounted for in the finite-a case, as well as on differences originating from variations in $\tau_{\min}$. Results are illustrated in figure 3, whose error bands encompass other fit forms as well, as described in appendix D.

We have repeated the analysis for the colour-electric correlator with pre-existing data and with a part of our new set, permitting for a direct comparison of the two transport coefficients. In this case, renormalization is perturbative [31], as non-perturbative renormalization factors have unfortunately not been worked out to date. The correlation functions are illustrated in figure 4, which also shows a comparison with NLO perturbative results from appendix C.

Our final results for the transport coefficients are collected in table 2 (the errors shown include the full spreads from figure 3). The electric and magnetic contributions have been combined according to [13]

$$\kappa \simeq \kappa_E + \frac{2}{3}\langle \mathbf{v}^2 \rangle\,\kappa_B\,, \tag{5.6}$$

---

[1]More precisely, the spectral function has the shape $\rho_B(\omega) = \frac{g^2(\bar{\mu})C_{\mathrm{F}}\,\omega^3}{6\pi}\Big\{1 + g^2(\bar{\mu})\big[(b_0 - \gamma_0)\ln\frac{\bar{\mu}^2}{\omega^2} + \gamma_0\ln\frac{\bar{\mu}^2}{(\pi T)^2} + c + f_T\big(\frac{\omega}{\pi T}\big)\big]\Big\}$, cf. eqs. (2.6) and (C.23), where f_T is power-suppressed at large values of $\omega/(\pi T)$. Eq. (5.4) follows by choosing the renormalization scale $\bar{\mu}$ so as to eliminate large logarithms.

[2]We have tested some of them, remaining with two fit parameters, and included the spread in our results. The tests are described in more detail in appendix D.
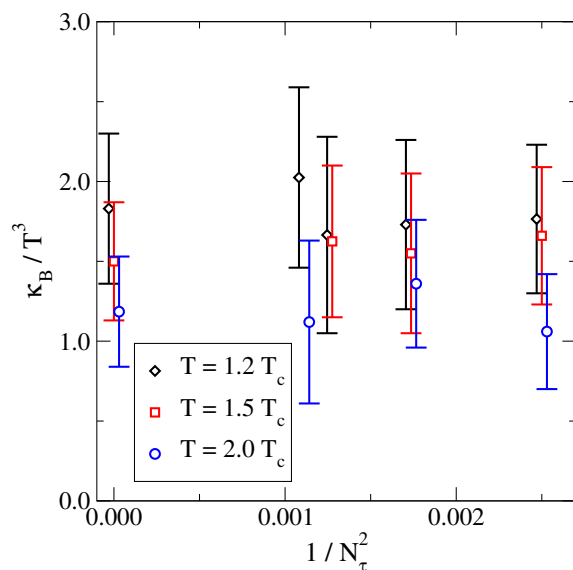
Figure 3. The parameter κ_B/T^3 as obtained from finite-a correlators, and separately from the continuum-extrapolated correlator. For better visibility, the data have been slightly displaced in the horizontal direction. Discretization uncertainties are modest compared with statistical ones.
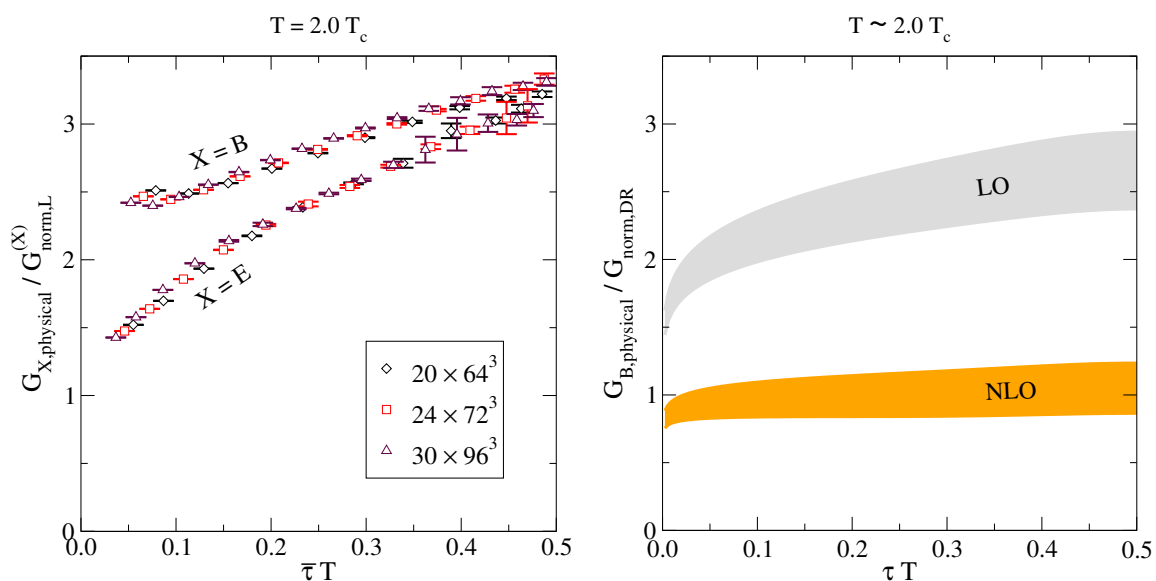

Figure 4. Left: comparison of the colour-magnetic and colour-electric correlators, at $T = 2.0T_c$ (improved distances and normalizations are different in the two cases, cf. appendix B). Right: the colour-magnetic correlator according to NLO perturbation theory, cf. appendix C. The lattice data suggests a large contribution on top of the NLO result (the latter shows poor convergence, which could be marginally improved upon by tuning the numerical factors in the scale choice in eq. (5.4)).

T/T_c	κ_E/T^3	κ_B/T^3	$\langle \mathbf{v}^2 \rangle_c$	$\langle \mathbf{v}^2 \rangle_b$	κ_c/T^3	κ_b/T^3	η_c/T	η_b/T
1.2	$1.5 - 3.4^*$	$1.0 - 2.6$	0.52	0.20	$1.8 - 4.3$	$1.6 - 3.8$	$0.16 - 0.38$	$0.05 - 0.13$
1.5	$1.3 - 2.8^*$	$1.0 - 2.1$	0.59	0.24	$1.7 - 3.7$	$1.4 - 3.2$	$0.16 - 0.36$	$0.05 - 0.13$
2.0	$1.0 - 2.5^*$	$0.6 - 1.8$	0.67	0.30	$1.2 - 3.4$	$1.1 - 2.9$	$0.14 - 0.37$	$0.05 - 0.15$

Table 2. Fit results for the contributions to κ from the colour-electric and colour-magnetic fields. Results for κ_E have been indicated with a star because measurements were only carried out on a subset of our lattices and thus some finite-volume and finite-a checks are missing. For comparison, a more comprehensive analysis suggests $\kappa_E/T^3 \simeq 1.8 - 3.4$ at $T/T_c = 1.5$ [9]. In order to combine the results according to eq. (5.6), the average thermal velocity is needed; this has been estimated from NLO results for the constant parts in the spatial and temporal vector current correlators [32]. The drag force η is obtained from eq. (5.8). The subscripts c,b refer to charm and bottom quarks.

which requires knowledge of the average thermal velocity. Within the T/M expansion, this can be expressed as [13]

$$\langle \mathbf{v}^2 \rangle \approx \frac{3T}{M_{\mathrm{kin}}} \left(1 - \frac{5T}{2M_{\mathrm{kin}}} \right), \tag{5.7}$$

however the value of the kinetic mass M_{kin} is ambiguous, and the large coefficient in the round brackets renders the convergence of the expansion questionable. An alternative definition of $\langle \mathbf{v}^2 \rangle$ can be given as the ratio of the almost constant (τ-independent) part of the spatial vector current correlator, and the susceptibility [5]. This definition does not rely on an expansion in T/M, and has been worked out up to NLO in the weak-coupling expansion [32]. The corresponding numerical values have been indicated in table 2.[3]

Given the value of κ, the drag force η appearing in eq. (1.1) can be obtained from a fluctuation-dissipation relation. A convenient way to express this, accurate up to NLO corrections in T/M_{kin} [13], reads

$$\eta \approx \frac{\kappa \langle \mathbf{v}^2 \rangle}{6T^2} . \tag{5.8}$$

This has also been shown in table 2. The traditional diffusion coefficient could similarly be estimated from $D \simeq 2T^2/\kappa$, however it plays no direct role in studies based on eq. (1.1).

6 Conclusions and outlook

The purpose of this paper has been to present a numerical simulation of the colour-magnetic correlator defined by eq. (2.1), followed by its non-perturbative renormalization (cf. eq. (2.9)) and extrapolation to the continuum limit (cf. section 4). Subjecting the result to simple-minded spectral modelling (cf. section 5), yields physical results as displayed in table 2.

A strength of our effective-theory approach, based on an expansion in T/M, is that the spectral function corresponding to eq. (2.1) is believed to be smooth at small $\omega \ll T$, i.e. free from a sharp transport peak. If the corresponding physics is addressed with a relativistic formulation instead, measuring vector current correlators, the spectral function

---

[3]Separate values for the numerator (i.e. spatial vector correlator) and denominator (i.e. susceptibility) can be found on the web page http://www.laine.itp.unibe.ch/quarkonium/.

has a transport peak of width $\eta \sim \alpha_{\rm s}^2 T^2 / M$ [33]. It has been suggested recently that employing a Lorentzian-shaped spectral function, of width η, in connection with lattice data, meaningful constraints on η can be extracted [34]. Specifically, table VI of ref. [34] cites $\eta_{\rm c}/T \simeq 0.9 - 5.3$ at $T/T_{\rm c} = 1.5 - 2.25$, and $\eta_{\rm b}/T \simeq 0.3 - 4.0$ at $T/T_{\rm c} = 1.3 - 2.25$. In view of table 2, it seems that these values are clearly on the high side, as is to be expected from the insufficient resolution of the relativistic formulation to narrow peaks.

We end by noting that the cost-effective results obtained with our approach suggest unquenched simulations as a goal for the future, whereas within the quenched approximation, systematic uncertainties deserve to be further scrutinized (cf. figures 1–3 and 5).

Acknowledgments

A   Non-perturbative renormalization of the colour-magnetic operator

We review here results for the non-perturbative renormalization of the colour-magnetic operator from ref. [18], incorporating minor modifications that are either necessary for our context, or would not be strictly necessary, but can be conveniently implemented, given that higher-order perturbative results have become available in the meanwhile.

Ref. [18] considered two possibilities for the propagation of the heavy quarks in the time direction. The case with just time-like links appearing, like in eq. (2.1), corresponds to the Eichten-Hill (EH) action.

The key result of ref. [18] is how the bare lattice operator for $[gB_i]_{\rm bare,L}$ from eq. (2.2) is related to the renormalization-group invariant (RGI) version of the same operator. This is expressed in its eq. (5.7) as

$$Z_{\rm spin}^{\rm RGI} = \frac{\Phi_{\rm RGI}}{\Phi_{\rm SF}\left(\frac{1}{2L_{\rm max}}\right)} \times Z_{\rm spin}^{\rm SF}(2L_{\rm max}) \,, \tag{A.1}$$

where $L_{\rm max}$ parametrizes a specific finite-volume Schrödinger functional (SF) scheme. The inverse of the first factor in eq. (A.1), which is a continuum quantity (i.e. with no reference to the lattice coupling), is given by eq. (5.6) of ref. [18]:

$$\frac{\Phi_{\rm SF}\left(\frac{1}{2L_{\rm max}}\right)}{\Phi_{\rm RGI}} = 0.992(29) \,. \tag{A.2}$$
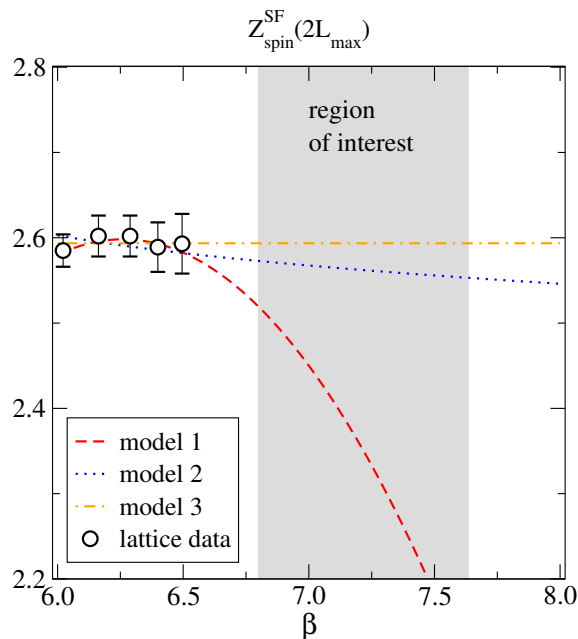
Figure 5. Shown are the lattice data from table 3 of ref. [18] (case EH), compared with the interpolation from eq. (A.3) [model 1] and the extrapolations from eqs. (A.4) and (A.5) [models 2 and 3]. The fit parameters read $k_0 \approx 2.66668$ and $k_1 \approx 2.59353$.

It is the second factor in eq. (A.1) which incorporates the dependence on the bare lattice coupling. With the step-scaling approach [35], $Z_{\mathrm{spin}}^{\mathrm{SF}}$ was measured for a number of β-values in ref. [18]. Furthermore, an interpolating function was suggested, as

$$Z_{\mathrm{spin}}^{\mathrm{SF}}(2L_{\mathrm{max}}) \overset{\mathrm{model\ 1}}{\approx} 2.58 + 0.14\,(\beta - 6) - 0.27(\beta - 6)^2\,, \tag{A.3}$$

where the denomination "model 1" is ours. However, this can only be used in the range $6.0 \leq \beta \leq 6.5$ where the measurements lie. We need to access the range $6.86 \leq \beta \leq 7.634$, and then eq. (A.3) cannot be applied.

To go to larger β, we can take inspiration from perturbation theory, even though it is not quantitatively accurate in this β-range. One possible representation would be to consider[4]

$$Z_{\mathrm{spin}}^{\mathrm{SF}}(2L_{\mathrm{max}}) \overset{\mathrm{model\ 2}}{\simeq} k_0 - \gamma_0 \ln\!\left(\frac{r_0}{a}\right)\frac{6}{\beta}\,, \tag{A.4}$$

with k_0 treated as a fit parameter and the anomalous dimension taking the value $\gamma_0 = 3/(8\pi^2)$. As another possible fit form, we consider

$$Z_{\mathrm{spin}}^{\mathrm{SF}}(2L_{\mathrm{max}}) \overset{\mathrm{model\ 3}}{\simeq} k_1\,, \tag{A.5}$$

which actually provides for a statistically better description of the data.

The resulting fits, and extrapolation towards large β, are illustrated in figure 5. It is clear that in the domain $6.86 \leq \beta \leq 7.634$, eq. (A.3) does not perform well, as it takes values

---

[4]We thank R. Sommer for suggesting this form.

far away from the interpolation data and has a shape very different from that expected at large β. Eqs. (A.4) and (A.5) may also incorporate substantial systematic uncertainties, but the difference of the results obtained with these two models is much smaller ($\lesssim 2\%$) than our statistical uncertainties (cf. figure 3). The results shown in this paper are based on model 2.

The remaining ingredient is how the RGI operator can be run down to an $\overline{\text{MS}}$ scale. Mirrorring eq. (5.4) of ref. [18], let us denote this factor by

$$\frac{\Phi_{\text{RGI}}}{\Phi_{\overline{\text{MS}}}(\bar{\mu})} = [2b_0 g^2(\bar{\mu})]^{-\frac{\gamma_0}{2b_0}} \exp\left\{-\int_0^{g(\bar{\mu})} dg'\left[\frac{\gamma(g')}{\beta(g')} - \frac{\gamma_0}{b_0 g'}\right]\right\}. \tag{A.6}$$

This factor is a function of $\bar{\mu}/\Lambda_{\overline{\text{MS}}}$, where $\bar{\mu}$ is the scale parameter of the $\overline{\text{MS}}$ scheme. Eqs. (6.7) and (6.8) of ref. [18] express the resulting conversion as

$$Z_{\text{spin}}^{\overline{\text{MS}}}(\bar{\mu}) = \frac{\Phi_{\overline{\text{MS}}}(\bar{\mu})}{\Phi_{\text{RGI}}} \times Z_{\text{spin}}^{\text{RGI}}, \tag{A.7}$$

citing for $\Phi_{\overline{\text{MS}}}(\bar{\mu})/\Phi_{\text{RGI}}$ the value 0.756(18) for the scale choice $\frac{\bar{\mu}}{\Lambda_{\overline{\text{MS}}}} = \frac{2\,\text{GeV}}{238\,\text{MeV}}$.[5]

For us, the key difference is that we need to run to the $\overline{\text{MS}}$ scale $\bar{\mu} \approx 19.179T$, as discussed around eq. (2.8). Recalling that $T_c/\Lambda_{\overline{\text{MS}}} = 1.24(10)$ [21], we therefore need to evaluate $\Phi_{\overline{\text{MS}}}(\bar{\mu})/\Phi_{\text{RGI}}$ with $\bar{\mu}/\Lambda_{\overline{\text{MS}}} \approx 19.179 \times 1.24 \times \frac{T}{T_c}$. This is typically somewhat larger than the scales considered in ref. [18], whereby we expect $\Phi_{\overline{\text{MS}}}(\bar{\mu})/\Phi_{\text{RGI}}$ to be smaller.

The numerical determination of $\Phi_{\overline{\text{MS}}}(\bar{\mu})/\Phi_{\text{RGI}}$ can in principle be done more precisely than in ref. [18], given that higher order corrections to the renormalization group equations have become available in the meanwhile. However, some care is needed in relating the conventions adopted by the pQCD and lattice communities. Denoting

$$a_s \equiv \frac{\alpha_s}{\pi} = \frac{g^2}{4\pi^2}, \quad \hat{t} \equiv \ln\left(\frac{\bar{\mu}^2}{\Lambda_{\overline{\text{MS}}}^2}\right), \tag{A.8}$$

the 5-loop evolution equation for a_s reads

$$\partial_{\hat{t}}\, a_s = -(\beta_0 a_s^2 + \ldots + \beta_4 a_s^6), \tag{A.9}$$

where ($N_c = 3$, $N_f = 0$) [36]

$$\beta_0 = \frac{11}{4}, \quad \beta_1 = \frac{51}{8}, \quad \beta_2 = \frac{2857}{128}, \quad \beta_3 = \frac{149753}{1536} + \frac{891\zeta_3}{64}, \tag{A.10}$$

$$\beta_4 = \frac{8157455}{16384} + \frac{621885\zeta_3}{2048} - \frac{88209\zeta_4}{2048} - \frac{144045\zeta_5}{512}. \tag{A.11}$$

The initial condition can be fixed at large $\hat{t} \equiv \hat{t}_{\max}$, e.g. $\hat{t}_{\max} = 200$, as

$$a_s(\hat{t}_{\max}) = \frac{1}{\beta_0 \hat{t}_{\max}} - \frac{\beta_1 \ln(\hat{t}_{\max})}{\beta_0^3 \hat{t}_{\max}^2} + \frac{\beta_0\beta_2 + \beta_1^2\left[\ln^2(\hat{t}_{\max}) - \ln(\hat{t}_{\max}) - 1\right]}{\beta_0^5 \hat{t}_{\max}^3} + \mathcal{O}\left(\frac{1}{\hat{t}_{\max}^4}\right), \tag{A.12}$$

which solves eq. (A.9) up to 3-loop order, and guarantees that $\Lambda_{\overline{\text{MS}}}$ has its standard meaning.

---

[5]The use of the relations is illustrated a few lines below eq. (6.8) in ref. [18], suggesting that for $\beta = 6$ and $\bar{\mu} = 2\,\text{GeV}$ the overall factor from eqs. (A.1)–(A.3) and (A.7) should be $0.756 \times 0.99 \times 2.58 = 1.93$. Unfortunately, there is a bug here, with a comparison of eqs. (A.1) and (A.2) indicating that the factor should be $0.756 \times 2.58/0.99 = 1.97$. We thank H.B. Meyer and R. Sommer for confirming our interpretation.

To relate these to eq. (A.6), we note that in eq. (A.6) the evolution equation for the running coupling has been assumed to have the form

$$\bar{\mu}\frac{\mathrm{d}g}{\mathrm{d}\bar{\mu}} = \beta(g) = -g^3\left(b_0 + b_1 g^2 + \ldots\right). \tag{A.13}$$

A comparison with eq. (A.9) yields

$$b_0 = \frac{\beta_0}{4\pi^2}, \quad b_1 = \frac{\beta_1}{(4\pi^2)^2}, \quad \ldots. \tag{A.14}$$

Now, making use of eq. (A.13), it is straightforward to verify that the ratio in eq. (A.6) satisfies

$$\bar{\mu}\frac{\mathrm{d}}{\mathrm{d}\bar{\mu}}\left[\frac{\Phi_{\mathrm{RGI}}}{\Phi_{\overline{\mathrm{MS}}}(\bar{\mu})}\right] = -\gamma(g)\left[\frac{\Phi_{\mathrm{RGI}}}{\Phi_{\overline{\mathrm{MS}}}(\bar{\mu})}\right], \tag{A.15}$$

where $\gamma(g)$ has the expansion

$$\gamma(g) = -g^2\left(\gamma_0 + \gamma_1 g^2 + \ldots\right). \tag{A.16}$$

In the notation of ref. [37], the corresponding quantity is γ_{cm}, given in its eq. (13),

$$\gamma_{\mathrm{cm}} = \tilde{\gamma}_0\, a_s + \tilde{\gamma}_1\, a_s^2 + \tilde{\gamma}_2\, a_s^3 + \ldots, \tag{A.17}$$

where ($N_{\mathrm{c}} = 3$, $N_{\mathrm{f}} = 0$) [37]

$$\tilde{\gamma}_0 = \frac{3}{2}, \quad \tilde{\gamma}_1 = \frac{17}{4}, \quad \tilde{\gamma}_2 = \frac{899}{64} + \frac{15\pi^2}{16} + \frac{27\zeta_3}{8}. \tag{A.18}$$

Recalling the definition of a_s from eq. (A.8), the relation of the couplings in eqs. (A.16) and (A.18) is

$$\gamma_0 = \frac{\tilde{\gamma}_0}{4\pi^2}, \quad \gamma_1 = \frac{\tilde{\gamma}_1}{(4\pi^2)^2}, \quad \ldots. \tag{A.19}$$

The initial condition for eq. (A.15) can be obtained from a perturbative solution of eq. (A.6). Denoting $g^2(\bar{\mu}_{\mathrm{max}}) \equiv 4\pi^2 a_s(\hat{t}_{\mathrm{max}})$, where $a_s(\hat{t}_{\mathrm{max}})$ is from eq. (A.12), this reads

$$\frac{\Phi_{\mathrm{RGI}}}{\Phi_{\overline{\mathrm{MS}}}(\bar{\mu}_{\mathrm{max}})} \approx [2b_0 g^2(\bar{\mu}_{\mathrm{max}})]^{-\frac{\gamma_0}{2b_0}} \exp\left\{-\frac{\gamma_0}{2b_0}\left(\frac{\gamma_1}{\gamma_0} - \frac{b_1}{b_0}\right) g^2(\bar{\mu}_{\mathrm{max}})\right\}. \tag{A.20}$$

Solving the coupled set of differential equations from eqs. (A.9) and (A.15), with the initial conditions from eqs. (A.12) and (A.20), and plotting the inverse of the result, as needed in eq. (A.7), we obtain the curve shown in figure 6. This is the result employed in our analysis.
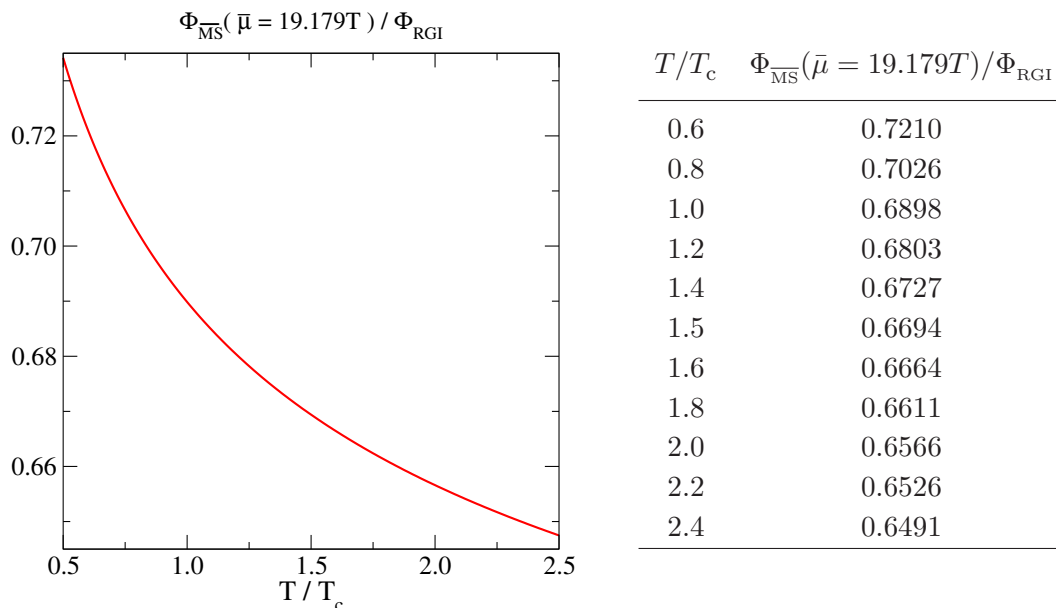
T/T_c	$\Phi_{\overline{\mathrm{MS}}}(\bar\mu = 19.179T)/\Phi_{\mathrm{RGI}}$
0.6	0.7210
0.8	0.7026
1.0	0.6898
1.2	0.6803
1.4	0.6727
1.5	0.6694
1.6	0.6664
1.8	0.6611
2.0	0.6566
2.2	0.6526
2.4	0.6491

Figure 6. Illustration of the conversion factor $\Phi_{\overline{\mathrm{MS}}}/\Phi_{\mathrm{RGI}}$, needed for pulling back an RGI-renormalized colour-magnetic field to the $\overline{\mathrm{MS}}$ scale $\bar\mu \approx 19.179T$ that is need in the thermal context (cf. eq. (2.8)).

B   Lattice perturbation theory and tree-level improvement

We have computed the correlator obtained with the discretization of eqs. (2.2)–(2.4) to leading order in lattice perturbation theory. The result differs slightly from the corresponding result for the colour-electric correlator [7], even if the continuum limit is the same. Denoting by N_τ the number of lattice points in the time direction, the new result reads

$$\left[G_B(\tau)\right]_{\mathrm{bare,L}}^{\mathrm{LO}} = \frac{g_0^2 C_{\mathrm{F}}}{3a^4} \int\limits_{-\pi}^{\pi} \frac{\mathrm{d}^3\mathbf{q}}{(2\pi)^3} \frac{\mathrm{e}^{\bar q N_\tau(1-\tau T)} + \mathrm{e}^{\bar q N_\tau \tau T}}{\mathrm{e}^{\bar q N_\tau} - 1} \frac{\tilde q^2 - \frac{(\tilde q^2)^2 + \tilde q^4}{8} + \frac{\tilde q^2 \tilde q^4 - \tilde q^6}{32}}{\sinh \bar q}, \qquad (\mathrm{B.1})$$

$$\bar q \equiv 2\,\mathrm{arsinh}\left(\frac{\sqrt{\tilde q^2}}{2}\right), \quad \tilde q^n \equiv \sum_{i=1}^{3} 2^n \sin^n\left(\frac{q_i}{2}\right). \qquad (\mathrm{B.2})$$

At this order the coupling g_0^2 denotes the bare lattice coupling, $g_0^2 \equiv 6/\beta$. For purposes of normalization, it is convenient to eliminate the dependence on the coupling, whence we define

$$G_{\mathrm{norm,L}}(\tau) \equiv \frac{\left[G_B(\tau)\right]_{\mathrm{bare,L}}^{\mathrm{LO}}}{g_0^2 C_{\mathrm{F}}}. \qquad (\mathrm{B.3})$$

The corresponding continuum correlator is given in eq. (4.1).

Eqs. (4.1) and (B.3) permit to implement "tree-level improvement" [20, 28], which can significantly reduce discretization effects at small distances. Using eqs. (4.1) and (B.3) to determine $\bar\tau$ from

$$G_{\mathrm{norm,DR}}(\bar\tau) \equiv G_{\mathrm{norm,L}}(\tau), \qquad (\mathrm{B.4})$$
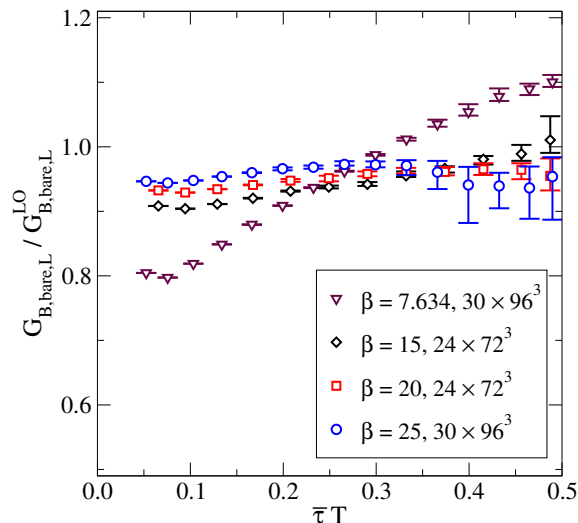
Figure 7. Approach of the lattice measurement towards the tree-level prediction in eq. (B.1). Shown is one of our production sets (without renormalization from eq. (2.9), which would be $\{\dots\}^2 \approx 2.871$) and, for comparison, three short runs in which the bare coupling $g_0^2 = 6/\beta$ was made extremely small.

the tree-level improved correlator is obtained from

$$\left[G_B(\bar{\tau})\right]_{\mathrm{bare,L}}^{\mathrm{imp}} \equiv \left[G_B(\tau)\right]_{\mathrm{bare,L}},\tag{B.5}$$

i.e. the measured values at distance τ are assigned to a corrected value $\bar{\tau}$.

Another use of the perturbative expression in eq. (B.1) is that it permits to crosscheck the overall normalization of the lattice measurement, by going to very large β. Results are shown in figure 7, and at short separations display a gradual movement towards unity as β increases, thereby confirming that everything is in order.

C Colour-magnetic spectral function at next-to-leading order

At next-to-leading order, the continuum diagrams contributing to $G_B(\tau)$ are those in figure 8.[6] The leading-order contribution reads

$$\delta_{(\mathrm{a})}G_B(\tau) = \frac{g_{\mathrm{B}}^2 C_{\mathrm{F}}(D-3)(D-2)}{3}\mathcal{J}_0(\tau),\tag{C.1}$$

where $D \equiv 4 - 2\epsilon$ is the space-time dimension, $\mathcal{J}_0$ is defined in eq. (C.8), and the bare coupling reads

$$g_{\mathrm{B}}^2 = g^2 + \frac{g^4\mu^{-2\epsilon}}{(4\pi)^2}\frac{2N_{\mathrm{f}} - 11N_{\mathrm{c}}}{3\epsilon} + \mathcal{O}(g^6).\tag{C.2}$$

---

[6]To simplify the notation we omit the specifier $[\dots]_{\mathrm{bare,DR}}$ in this section.
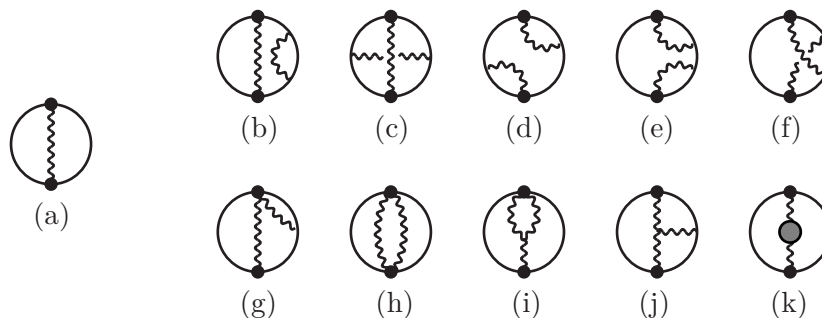
Figure 8. The Feynman diagrams contributing to the continuum version of the colour-magnetic correlator defined in eq. (2.1). The circle illustrates a Polyakov loop, the wavy lines are gluons, the small dots stand for insertions of B_i, and the grey blob is the gluon self-energy.

At next-to-leading order, following a numbering for "master" structures adopted from refs. [13, 30], the non-vanishing contributions of the individual graphs read

$$\delta_{(a)}G_B(\tau) \times \frac{\chi_{\text{LO}}}{\chi_{\text{NLO}}} + \delta_{(b\text{-}f)}G_B(\tau) = \frac{g^4 N_c C_F(D-3)(D-2)}{3} \mathcal{I}_4(\tau) \,, \tag{C.3}$$

$$\delta_{(h)}G_B(\tau) = \frac{g^4 N_c C_F(D-3)(D-2)(D-1)}{6} \mathcal{I}_1(\tau) \,, \tag{C.4}$$

$$\delta_{(i)}G_B(\tau) = -g^4 N_c C_F(D-3)(D-2) \mathcal{I}_2(\tau) \,, \tag{C.5}$$

$$\delta_{(j)}G_B(\tau) = \frac{g^4 N_c C_F(D-3)(D-2)}{6} \mathcal{I}_6(\tau) \,, \tag{C.6}$$

$$\delta_{(k)}G_B(\tau) = \frac{g^4 C_F(D-3)}{3} \left\{ (D-2)N_c \left[-\frac{(D-2)(D-1)}{2} \mathcal{I}_0(\tau) + 2\mathcal{I}_2(\tau) + 2\mathcal{I}_7(\tau) \right] \right. $$
$$\left. + N_f \left[(D-2)(D-1)\mathcal{I}_{\{0\}}(\tau) - (D-2)\mathcal{I}_{\{2\}}(\tau) - 4\mathcal{I}_{\{7\}}(\tau) \right] \right\}. \tag{C.7}$$

Here χ refers to the denominator of eq. (2.1).

As Matsubara sum-integrals, or in terms of a configuration-space representation in the case of eq. (C.13), the master structures are defined as

$$\mathcal{J}_0(\tau) \equiv \oint_K \frac{k^2 e^{ik_n\tau}}{K^2} \,, \tag{C.8}$$

$$\mathcal{I}_0(\tau) \equiv \oint_{K,Q} \frac{e^{ik_n\tau}}{K^2(K-Q)^2} \,, \tag{C.9}$$

$$\mathcal{I}_1(\tau) \equiv \oint_{K,Q} \frac{e^{ik_n\tau}}{Q^2(K-Q)^2} \,, \tag{C.10}$$

$$\mathcal{I}_2(\tau) \equiv \oint_{K,Q} \frac{k^2 e^{ik_n\tau}}{K^2 Q^2(K-Q)^2} \,, \tag{C.11}$$

$$\mathcal{I}_4(\tau) \equiv \oint_K \frac{k^2 e^{ik_n\tau}}{K^2} \oint_{Q'} \frac{e^{iq_n\tau}-1}{q_n^2 Q^2} \,, \tag{C.12}$$

– 16 –

$$\mathcal{I}_6(\tau) \equiv \left[\int_\tau^\beta \mathrm{d}\tau' - \int_0^\tau \mathrm{d}\tau'\right]\int_X G(X - \tau'\mathbf{e}_0)$$

$$\times \left[\partial_i G(X - \tau\mathbf{e}_0)\,\partial_0\partial_i G(X) - \partial_0\partial_i G(X - \tau\mathbf{e}_0)\,\partial_i G(X)\right], \tag{C.13}$$

$$\mathcal{I}_7(\tau) \equiv -\lim_{\lambda \to 0}\frac{\mathrm{d}}{\mathrm{d}\lambda^2}\oint_{K,Q}\frac{[k^2 q^2 - (\mathbf{k}\cdot\mathbf{q})^2]e^{ik_n\tau}}{(K^2 + \lambda^2)Q^2(K - Q)^2}\,, \tag{C.14}$$

where for eq. (C.13) we have defined $G(X) \equiv \oint_K e^{iK\cdot X}/K^2$. Moreover, the notation $\mathcal{I}_{\{i\}}$ implies that the thermal distribution is fermionic (cf. the line after eq. (C.22)).

To obtain the spectral function, we go over to frequency space, carry out an analytic continuation, and take the cut,

$$\tilde{\mathcal{I}}_i(\omega) \equiv \mathrm{Im}\left[\int_0^{1/T}\mathrm{d}\tau\, e^{ik_n\tau}\,\mathcal{I}_i(\tau)\right]_{k_n \to -i[\omega + i0^+]}. \tag{C.15}$$

Employing techniques explained in ref. [30], this leads to the integral representations

$$\tilde{\mathcal{J}}_0(\omega) = \frac{\omega^3\mu^{-2\epsilon}}{4\pi}\left[1 + \epsilon\left(\ln\frac{\bar{\mu}^2}{4\omega^2} + 2\right)\right] + \mathcal{O}(\epsilon^2)\,, \tag{C.16}$$

$$\tilde{\mathcal{I}}_0(\omega) = \frac{1}{16\pi^3}\int_0^\infty \mathrm{d}q\, n(q)[2q\omega] + \mathcal{O}(\epsilon)\,, \tag{C.17}$$

$$\tilde{\mathcal{I}}_1(\omega) = \frac{\omega^3\mu^{-4\epsilon}}{16\pi^3}\left(\frac{1}{6}\right) + \frac{1}{16\pi^3}\int_0^\infty \mathrm{d}q\, n(q)[4q\omega] + \mathcal{O}(\epsilon)\,, \tag{C.18}$$

$$\tilde{\mathcal{I}}_2(\omega) = \frac{\omega^3\mu^{-4\epsilon}}{16\pi^3}\left(\frac{1}{4\epsilon} + \frac{1}{2}\ln\frac{\bar{\mu}^2}{4\omega^2} + \frac{5}{3}\right)$$

$$+ \frac{1}{16\pi^3}\int_0^\infty \mathrm{d}q\, n(q)\left[4q\omega + \omega^2\ln\left|\frac{q + w}{q - w}\right|\right] + \mathcal{O}(\epsilon)\,, \tag{C.19}$$

$$\tilde{\mathcal{I}}_4(\omega) = \frac{\omega^3\mu^{-4\epsilon}}{16\pi^3}\left(\frac{1}{2\epsilon} + \ln\frac{\bar{\mu}^2}{4\omega^2} + \frac{23}{6}\right)$$

$$- \frac{1}{16\pi^3}\int_0^\infty \mathrm{d}q\, n(q)\left[4q\omega + \mathbb{P}\left(\frac{2q\omega^3}{\omega^2 - q^2}\right)\right] + \mathcal{O}(\epsilon)\,, \tag{C.20}$$

$$\tilde{\mathcal{I}}_6(\omega) = \frac{\omega^3\mu^{-4\epsilon}}{16\pi^3}\left(\frac{1}{2\epsilon} + \ln\frac{\bar{\mu}^2}{4\omega^2} + \frac{16}{3} - \frac{4\pi^2}{3}\right)$$

$$+ \frac{1}{8\pi^3}\int_0^\infty \mathrm{d}q\, n(q)\,\mathbb{P}\left\{4q\omega\left(1 + \frac{\omega^2}{\omega^2 - q^2}\right) + 5\omega^2\ln\left|\frac{q + \omega}{q - \omega}\right|\right.$$

$$\left. + \frac{2\omega^4}{q}\left[\frac{1}{q + \omega}\ln\frac{q + \omega}{\omega} - \frac{1}{q - \omega}\ln\frac{|q - \omega|}{\omega}\right]\right\} + \mathcal{O}(\epsilon)\,, \tag{C.21}$$

$$\tilde{\mathcal{I}}_7(\omega) = \frac{\omega^3\mu^{-4\epsilon}}{16\pi^3}\left(-\frac{1}{24\epsilon} - \frac{1}{12}\ln\frac{\bar{\mu}^2}{4\omega^2} - \frac{19}{72}\right)$$

$$+ \frac{1}{16\pi^3}\int_0^\infty \mathrm{d}q\, n(q)\left\{q^2\ln\left|\frac{q + \omega}{q - \omega}\right| + q\omega\ln\left|\frac{q^2 - \omega^2}{\omega^2}\right|\right\} + \mathcal{O}(\epsilon)\,, \tag{C.22}$$

where $\mathbb{P}$ denotes a principal value, and $n \equiv n_{\mathrm{B}}$ for bosons and $n \equiv -n_{\mathrm{F}}$ for fermions.

fit form	$N_\tau = 20$	$N_\tau = 24$	$N_\tau = 28$	$N_\tau = 30$	$N_\tau \to \infty$
eq. (5.5)	$1.30 - 1.94$	$1.20 - 1.75$	$1.09 - 1.82$	$1.56 - 2.00$	$1.56 - 1.82$
eq. (D.1)	$1.63 - 2.23$	$1.50 - 2.26$	$1.44 - 2.28$	$2.01 - 2.59$	$1.79 - 2.30$
eq. (D.2)	$1.30 - 1.90$	$1.20 - 1.66$	$1.05 - 1.67$	$1.46 - 2.01$	$1.36 - 1.75$
eq. (D.3)	$1.56 - 2.19$	$1.43 - 2.13$	$1.30 - 2.18$	$1.88 - 2.51$	$1.71 - 2.14$

Table 3. Fit results for κ_B/T^3 at $T = 1.2T_{\rm c}$, as described in appendix D.

Inserting the integral representations into the individual terms, summing them together, and going over to the $\overline{\rm MS}$ scheme according to eq. (2.5), the final result becomes

$$
\begin{aligned}
\left[\rho_B(\omega)\right]_{{\rm renorm},\bar\mu} =\ & \frac{g^2 C_{\rm F}\,\omega^3}{6\pi} \\
& \times \left\{ 1 + \frac{g^2}{(4\pi)^2}\left[N_{\rm c}\left(\frac{5}{3}\ln\frac{\bar\mu^2}{4\omega^2} + \frac{134}{9} - \frac{8\pi^2}{3}\right) - N_{\rm f}\left(\frac{2}{3}\ln\frac{\bar\mu^2}{4\omega^2} + \frac{26}{9}\right)\right]\right\} \\
& + \frac{g^4 C_{\rm F}}{12\pi^3}\Bigg\{ N_{\rm c}\int_0^\infty {\rm d}q\, n_{\rm B}(q)\, \mathbb{P}\left[(q^2 + 2\omega^2)\ln\left|\frac{q+w}{q-w}\right|\right. \\
& \qquad +\ q\omega\left(\ln\frac{|q^2-\omega^2|}{\omega^2} + \frac{\omega^2}{\omega^2-q^2} - 2\right) \\
& \qquad +\ \frac{\omega^4}{q}\left(\frac{1}{q+\omega}\ln\frac{q+\omega}{\omega} + \frac{1}{q-\omega}\ln\frac{\omega}{|q-\omega|}\right)\Bigg] \\
& \qquad +\ N_{\rm f}\int_0^\infty {\rm d}q\, n_{\rm F}(q)\left[\left(q^2 + \frac{\omega^2}{2}\right)\ln\left|\frac{q+w}{q-w}\right|\right. \\
& \qquad +\ q\omega\left(\ln\frac{|q^2-\omega^2|}{\omega^2} - 1\right)\Bigg]\Bigg\} + \mathcal{O}(g^6)\,.
\end{aligned}
\tag{C.23}
$$

The "physical" spectral function, appearing in eq. (5.1), involves a multiplication of this expression through c_B^2, cf. eq. (2.6). The IR limit agrees with an expression given in ref. [13],

$$
\begin{aligned}
\rho_B(\omega) \overset{\omega\ll\pi T}{\approx}\ & \frac{g^4 C_{\rm F} T^2\omega}{36\pi}\Bigg\{ N_{\rm c}\left[\ln\left(\frac{T}{\omega}\right) + 1 - \gamma_{\rm E} + \frac{\zeta'(2)}{\zeta(2)}\right] \\
& + \frac{N_{\rm f}}{2}\left[\ln\left(\frac{2T}{\omega}\right) + \frac{3}{2} - \gamma_{\rm E} + \frac{\zeta'(2)}{\zeta(2)}\right]\Bigg\} + \mathcal{O}(g^6)\,.
\end{aligned}
\tag{C.24}
$$

D Details of spectral fitting procedure

We give here more details on the fitting procedure employed in section 5, which in the end produced the results shown in figure 3, after combining all errors in the most conservative way (from absolute minimum among the different fit forms, to the absolute maximum).

Four different forms have been employed for the spectral function: eq. (5.5), as well as

$$
\rho_B^{({\rm D.1})}(\omega) \equiv \max\{\phi_{\rm IR}(\omega), b_{B1}\,\phi_{\rm UV}(\omega)\}\,,
\tag{D.1}
$$

$$
\rho_B^{({\rm D.2})}(\omega) \equiv \left(1 + b_{B2}\sin\pi y\right)\sqrt{\phi_{\rm IR}^2(\omega) + \phi_{\rm UV}^2(\omega)}\,,
\tag{D.2}
$$

$$
\rho_B^{({\rm D.3})}(\omega) \equiv \left(1 + b_{B3}\sin\pi y\right)\max\{\phi_{\rm IR}(\omega), \phi_{\rm UV}(\omega)\}\,.
\tag{D.3}
$$

fit form	$N_\tau = 20$	$N_\tau = 24$	$N_\tau = 28$	$N_\tau \to \infty$
eq. (5.5)	$1.31 - 1.76$	$1.22 - 1.64$	$1.15 - 1.67$	$1.18 - 1.67$
eq. (D.1)	$1.70 - 2.09$	$1.41 - 2.05$	$1.38 - 2.10$	$1.32 - 1.87$
eq. (D.2)	$1.23 - 1.68$	$1.05 - 1.49$	$1.16 - 1.64$	$1.13 - 1.38$
eq. (D.3)	$1.60 - 1.99$	$1.36 - 1.92$	$1.25 - 1.94$	$1.31 - 1.81$

Table 4. Fit results for κ_B/T^3 at $T = 1.5T_{\rm c}$, as described in appendix D.
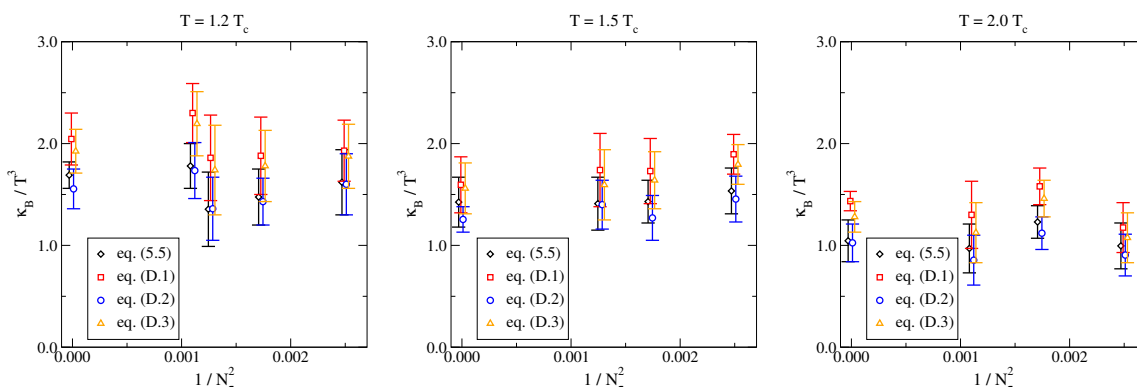
Figure 9. The parameter κ_B/T^3 as obtained from the different fits, according to tables 3–5. For better visibility, the data have been slightly displaced in the horizontal direction.

fit form	$N_\tau = 20$	$N_\tau = 24$	$N_\tau = 30$	$N_\tau \to \infty$
eq. (5.5)	$0.77 - 1.22$	$1.07 - 1.39$	$0.73 - 1.21$	$0.84 - 1.25$
eq. (D.1)	$0.93 - 1.42$	$1.40 - 1.76$	$0.97 - 1.63$	$1.34 - 1.53$
eq. (D.2)	$0.70 - 1.11$	$0.96 - 1.28$	$0.61 - 1.10$	$0.84 - 1.21$
eq. (D.3)	$0.83 - 1.32$	$1.28 - 1.64$	$0.83 - 1.42$	$1.13 - 1.43$

Table 5. Fit results for κ_B/T^3 at $T = 2.0T_{\rm c}$, as described in appendix D.

In the last two cases, following ref. [9], we have defined

$$x \equiv \ln\left(1 + \frac{\omega}{\pi T}\right), \quad y \equiv \frac{x}{1 + x}, \tag{D.4}$$

thereby mapping the ω-range $(0, \infty)$ onto the interval $(0, 1)$ such that at both ends the ω-dependence has a qualitatively reasonable form. The auxiliary fit parameters a_B, b_{B1} are of order unity, whereas b_{B2}, b_{B3} are in the range $0.02 - 0.10$. Our main interest is in the fit parameter κ_B/T^3, which enters through $\phi_{\rm IR}$ (cf. eq. (5.3)).

Since the continuum extrapolation, as described in section 4, involves various interpolations, with their own sets of uncertainties, we fit separately to the correlators at finite N_τ, in addition to the continuum-extrapolated correlators.

At $1.2T_{\rm c}$, we have four lattice spacings. The results are shown in table 3 and in the left panel of figure 9. In each case the fit was carried out for $\bar{\tau} \in (\bar{\tau}_{\rm low}, 0.5/T)$, where

$\bar{\tau}_{\text{low}}$ was varied in the range $\sim (0.25 - 0.35)/T$ for finite N_τ and $\bar{\tau}_{\text{low}} \sim 0.17/T$ for the continuum-extrapolated results. The error was obtained from a bootstrap analysis. The median of the bootstrap distribution of $\chi^2/\text{d.o.f.}$ was comfortably < 1.0, and always below ~ 1.5. The error bands include, besides this bootstrap error, the spread due to changing $\bar{\tau}_{\text{low}}$.

At $1.5T_c$ and $2.0T_c$, we have three lattice spacings. The results are shown in tables 4 and 5 and in the two right-most panels of figure 9, respectively. In each case the fit was carried out for $\bar{\tau} \in (\bar{\tau}_{\text{low}}, 0.5/T)$, where $\bar{\tau}_{\text{low}}$ was varied in the range $\sim (0.20 - 0.35)/T$, where $\chi^2/\text{d.o.f.}$ was acceptable. The interpretation of the error bands is similar to that at $1.2T_c$.

References

[1] R. Rapp et al., *Extraction of heavy-flavor transport coefficients in QCD matter*, *Nucl. Phys. A* **979** (2018) 21 [arXiv:1803.03824] [INSPIRE].

[2] B. Svetitsky, *Diffusion of charmed quarks in the quark-gluon plasma*, *Phys. Rev. D* **37** (1988) 2484 [INSPIRE].

[3] G.D. Moore and D. Teaney, *How much do heavy quarks thermalize in a heavy ion collision?*, *Phys. Rev. C* **71** (2005) 064904 [hep-ph/0412346] [INSPIRE].

[4] J. Casalderrey-Solana and D. Teaney, *Heavy quark diffusion in strongly coupled $\mathcal{N} = 4$ Yang-Mills*, *Phys. Rev. D* **74** (2006) 085012 [hep-ph/0605199] [INSPIRE].

[5] S. Caron-Huot, M. Laine and G.D. Moore, *A way to estimate the heavy quark thermalization rate from the lattice*, *JHEP* **04** (2009) 053 [arXiv:0901.1195] [INSPIRE].

[6] H.B. Meyer, *The errant life of a heavy quark in the quark-gluon plasma*, *New J. Phys.* **13** (2011) 035008 [arXiv:1012.0234] [INSPIRE].

[7] A. Francis, O. Kaczmarek, M. Laine and J. Langelage, *Towards a non-perturbative measurement of the heavy quark momentum diffusion coefficient*, *PoS* **LATTICE2011** (2011) 202 [arXiv:1109.3941] [INSPIRE].

[8] D. Banerjee, S. Datta, R. Gavai and P. Majumdar, *Heavy quark momentum diffusion coefficient from lattice QCD*, *Phys. Rev. D* **85** (2012) 014510 [arXiv:1109.5738] [INSPIRE].

[9] A. Francis, O. Kaczmarek, M. Laine, T. Neuhaus and H. Ohno, *Nonperturbative estimate of the heavy quark momentum diffusion coefficient*, *Phys. Rev. D* **92** (2015) 116003 [arXiv:1508.04543] [INSPIRE].

[10] N. Brambilla, V. Leino, P. Petreczky and A. Vairo, *Lattice QCD constraints on the heavy quark diffusion coefficient*, *Phys. Rev. D* **102** (2020) 074503 [arXiv:2007.10078] [INSPIRE].

[11] L. Altenkort, A.M. Eller, O. Kaczmarek, L. Mazur, G.D. Moore and H.-T. Shu, *Heavy quark momentum diffusion from the lattice using gradient flow*, *Phys. Rev. D* **103** (2021) 014511 [arXiv:2009.13553] [INSPIRE].

[12] L. Altenkort, A.M. Eller, O. Kaczmarek, L. Mazur, G.D. Moore and H.-T. Shu, *Spectral reconstruction details of a gradient-flowed color-electric correlator*, *EPJ Web Conf.* **259** (2022) 10004 [arXiv:2109.11303] [INSPIRE].

[13] A. Bouttefeux and M. Laine, *Mass-suppressed effects in heavy quark diffusion*, *JHEP* **12** (2020) 150 [arXiv:2010.07316] [INSPIRE].

[14] M. Laine, *1-loop matching of a thermal Lorentz force*, *JHEP* **06** (2021) 139 [arXiv:2103.14270] [INSPIRE].

[15] J. Mayer-Steudte, N. Brambilla, V. Leino and P. Petreczky, *Chromoelectric and chromomagnetic correlators at high temperature from gradient flow*, *PoS* **LATTICE2021** (2022) 318 [arXiv:2111.10340] [INSPIRE].

[16] L. Altenkort, A.M. Eller, O. Kaczmarek, L. Mazur, G.D. Moore and H.-T. Shu, *Continuum extrapolation of the gradient-flowed color-magnetic correlator at $1.5\,T_c$*, *PoS* **LATTICE2021** (2022) 367 [arXiv:2111.12462] [INSPIRE].

[17] E. Eichten and B. Hill, *Static effective field theory: $1/m$ corrections*, *Phys. Lett. B* **243** (1990) 427 [INSPIRE].

[18] D. Guazzini, H.B. Meyer and R. Sommer, *Non-perturbative renormalization of the chromo-magnetic operator in Heavy Quark Effective Theory and the B* - B mass splitting*, *JHEP* **10** (2007) 081 [arXiv:0705.1809] [INSPIRE].

[19] M. Dalla Brida, L. Giusti, T. Harris, D. Laudicina and M. Pepe, *Non-perturbative thermal QCD at all temperatures: the case of mesonic screening masses*, *JHEP* **04** (2022) 034 [arXiv:2112.05427] [INSPIRE].

[20] R. Sommer, *A new way to set the energy scale in lattice gauge theories and its applications to the static force and α_s in* SU(2) *Yang-Mills theory*, *Nucl. Phys. B* **411** (1994) 839 [hep-lat/9310022] [INSPIRE].

[21] A. Francis, O. Kaczmarek, M. Laine, T. Neuhaus and H. Ohno, *Critical point and scale setting in* SU(3) *plasma: An update*, *Phys. Rev. D* **91** (2015) 096002 [arXiv:1503.05652] [INSPIRE].

[22] Y. Burnier et al., *Thermal quarkonium physics in the pseudoscalar channel*, *JHEP* **11** (2017) 206 [arXiv:1709.07612] [INSPIRE].

[23] M. Lüscher and P. Weisz, *Locality and exponential error reduction in numerical lattice gauge theory*, *JHEP* **09** (2001) 010 [hep-lat/0108014] [INSPIRE].

[24] H.B. Meyer, *Calculation of the shear viscosity in* SU(3) *gluodynamics*, *Phys. Rev. D* **76** (2007) 101701 [arXiv:0704.1801] [INSPIRE].

[25] U. Wolff, *Monte Carlo errors with less errors*, *Comput. Phys. Commun.* **156** (2004) 143 [*Erratum ibid.* **176** (2007) 383] [hep-lat/0306017] [INSPIRE].

[26] S. Schaefer et al., *Critical slowing down and error analysis in lattice QCD simulations*, *Nucl. Phys. B* **845** (2011) 93 [arXiv:1009.5228] [INSPIRE].

[27] M. Lüscher, *Properties and uses of the Wilson flow in lattice QCD*, *JHEP* **08** (2010) 071 [*Erratum ibid.* **03** (2014) 092] [arXiv:1006.4518] [INSPIRE].

[28] H.B. Meyer, *Cutoff effects on energy-momentum tensor correlators in lattice gauge theory*, *JHEP* **06** (2009) 077 [arXiv:0904.1806] [INSPIRE].

[29] M. Laine, G.D. Moore, O. Philipsen and M. Tassler, *Heavy quark thermalization in classical lattice gauge theory: lessons for strongly-coupled QCD*, *JHEP* **05** (2009) 014 [arXiv:0902.2856] [INSPIRE].

[30] Y. Burnier, M. Laine, J. Langelage and L. Mether, *Colour-electric spectral function at next-to-leading order*, *JHEP* **08** (2010) 094 [arXiv:1006.0867] [InSPIRE].

[31] C. Christensen and M. Laine, *Perturbative renormalization of the electric field correlator*, *Phys. Lett. B* **755** (2016) 316 [arXiv:1601.01573] [InSPIRE].

[32] Y. Burnier and M. Laine, *Massive vector current correlator in thermal QCD*, *JHEP* **11** (2012) 086 [arXiv:1210.1064] [InSPIRE].

[33] P. Petreczky and D. Teaney, *Heavy quark diffusion from the lattice*, *Phys. Rev. D* **73** (2006) 014508 [hep-ph/0507318] [InSPIRE].

[34] H.-T. Ding, O. Kaczmarek, A.-L. Lorenz, H. Ohno, H. Sandmeyer and H.-T. Shu, *Charm and beauty in the deconfined plasma from quenched lattice QCD*, *Phys. Rev. D* **104** (2021) 114508 [arXiv:2108.13693] [InSPIRE].

[35] M. Lüscher, R. Narayanan, P. Weisz and U. Wolff, *The Schrödinger functional — a renormalizable probe for non-abelian gauge theories*, *Nucl. Phys. B* **384** (1992) 168 [hep-lat/9207009] [InSPIRE].

[36] P.A. Baikov, K.G. Chetyrkin and J.H. Kühn, *Five-Loop Running of the QCD Coupling Constant*, *Phys. Rev. Lett.* **118** (2017) 082002 [arXiv:1606.08659] [InSPIRE].

[37] A.G. Grozin, P. Marquard, J.H. Piclum and M. Steinhauser, *Three-loop chromomagnetic interaction in HQET*, *Nucl. Phys. B* **789** (2008) 277 [arXiv:0707.1388] [InSPIRE].